Assembly Process and Electrical Properties of Top-Transferred Graphene on Carbon Nanotubes for Carbon-Based 3-D Interconnects

Ye Zhu, Chong Wei Tan, Shen Lin Chua, Yu Dian Lim, Boris Vaisband, Beng Kang Tay, *Senior Member, IEEE*, Eby G. Friedman, *Fellow, IEEE*, and Chuan Seng Tan, *Senior Member, IEEE*

***Abstract*— Carbon nanomaterials, graphene, and carbon nanotubes (CNTs) have emerged as promising materials for the integration of future advance packaging technologies. The main benefits of carbon nanomaterials include excellent electrical, thermal, and mechanical properties. In this article, the transfer process of a top graphene layer onto the as-grown CNT bundles was successfully performed with direct graphene-to-CNT contact at the interface. Four-point-probe (4PP) *I–V* characterization suggests that an ohmic contact was achieved between the graphene and CNTs. Low CNT bump resistance of 2.1 Ω for 90 000-μm^2 CNT area including the CNT–graphene contact resistance was obtained, demonstrating a reduction in the contact resistance between the CNT and Au under the same fabrication and measurement conditions. This work presents the preliminary results for the assembly process of top-transferred graphene on the CNTs and the electrical properties of direct CNT–graphene contact, paving the way for the implementation of full-carbon-based three-dimensional (3-D) interconnects.**

***Index Terms*— Carbon nanotube (CNT), graphene, three-dimensional (3-D) interconnects.**

I. Introduction

THE continuous miniaturization of integrated circuits (ICs) as driven by Moore's law results in progressive performance improvement and cost reduction in electronic products over the past 40 years [1]. In recent years, however, this progressive trend has been constrained as the device scaling reaches the fundamental physical limitations. The escalating cost of Moore's law has pivoted the semiconductor industry's focus to "More-than-Moore (MtM)" technologies [2]. Supported by advanced packaging solutions, high-density heterogeneous integration of analog/mixed-signal, RF, microelectromechanical system (MEMS), and image sensing with CMOS in a variety of 2.5-D and 3-D architectures is expected to be the main driving forces for the next-generation electronic products [3].

Vertical stacking of the IC layers to form 3-D integration is one of the recent focuses in the advanced electronic packaging techniques [4], [5]. Apart from higher integration density obtained by 3-D stacking, it can also achieve a complete functional unit by system-in-package integration. To realize this, reliable and efficient electrical interconnects for signal transmission and power distribution are needed [6]. Among the signal transmission techniques, flip chip bump and through-silicon via (TSV) technologies have been used for the vertical interconnections between the chip and the substrate. The flip chip bumps are able to achieve higher input–output (I/O) counts due to short electrical connection paths [7], whereas the TSV technology enables faster, short-path communication channeling between the vertically stacked ICs and devices [8].

A technical challenge in the existing flip chip bumps and TSVs is the difference in the coefficient of thermal expansion (CTE) between the copper bump/TSV-filler and its surrounding materials. Due to the relatively large CTE mismatch between silicon (2.3×10^{-6}/°C) and copper (17×10^{-6}/°C) [9], [10], the Cu-based pillar bumps and TSVs fabricated on the Si substrate raise numerous stability and reliability issues during chip operation, especially in the fluctuated temperature conditions.

Carbon nanomaterials, graphene, and carbon nanotubes (CNTs) have emerged as promising materials for the integration in the next-generation advanced packaging technologies [11], [12]. The main benefit of carbon nanomaterials, for example, CNTs, lies in their excellent electrical, thermal, and mechanical properties: 1) low electrical resistivity, measured in a range of 0.8–33.8 m$\Omega \cdot$cm for single CNT and CNT bundles [13]–[15]; 2) high current density $\sim 10^9$ A/cm^2 in single CNT [16]; 3) high thermal conductivity, reported in a range of 600–3000 W/mK for individual multi-walled CNTs (MWCNTs) [17]–[20]; and 4) closer CTE to Si (2.3×10^{-6}/°C) when compared with Cu (17×10^{-6}/°C), for example, $\sim 2 \times 10^{-6}$/°C for single-walled CNTs (SWCNTs) [21]. At the same time, the porous structure of the CNT bundles eases the thermal mismatch

Manuscript received June 15, 2019; revised August 17, 2019; accepted August 23, 2019. Date of publication September 11, 2019; date of current version March 10, 2020. This work was supported by the Ministry of Education (MOE) Tier-2 under Grant #MOE2014-T2-2-105 (ARC22/15). Recommended for publication by Associate Editor P. Franzon upon evaluation of reviewers' comments. *(Corresponding author: Ye Zhu.)*

Y. Zhu, C. W. Tan, S. L. Chua, Y. D. Lim, B. K. Tay, and C. S. Tan are with the School of Electrical and Electronic Engineering, Nanyang Technological University, Singapore 639798 (e-mail: yzhu012@e.ntu.edu.sg; tancs@ntu.edu.sg).

B. Vaisband is with the Department of Electrical and Computer Engineering, University of California at Los Angeles, Los Angeles, CA 90095 USA

E. G. Friedman is with the Department of Electrical and Computer Engineering, University of Rochester, Rochester, NY 14627 USA.

Color versions of one or more of the figures in this article are available online at http://ieeexplore.ieee.org.

Digital Object Identifier 10.1109/TCPMT.2019.2940511

stress introduced in the surrounding Si substrate [9]. These advantages enable the carbon nanomaterials to be highly attractive candidates as both on-chip and off-chip interconnects in 3-D integration. Currently, substantial works have been done for the fabrication and characterization of CNT TSVs on conductive metal lines [22], [23]. Meanwhile, the CNT bumps have been demonstrated as the potential flip chip bumps by several groups [24]–[26]. Apart from the CNTs, graphene has also been proposed as a potential candidate to replace copper as the next-generation planar interconnects due to its patterning feasibility and high current mobility [27]–[30].

Besides the thermal mismatch issue, full-carbon-based interconnects are expected to have better out-of-plane and in-plane electrical properties when compared with their copper counterparts [31]. It has been demonstrated that the full integration of the intercalation-doped multi-layer graphene (MLG) wires and the CNTs offers better electrical performance reliability when compared with the Cu interconnects at 5-nm node [32]. Another successful fabrication of the graphene–CNT heterostructure for the off-chip interconnects has been made through a direct growth of the CNTs within the vias, on top of the graphene [33]. To form a complete bottom–up full-carbon 3-D interconnection, the assembly process of the top graphene layer after the CNT growth needs be explored. Meanwhile, the electrical properties of the contact formed between the CNTs and the top graphene layer after the assembly process require further investigations.

In this work, we have successfully performed an assembly process by transferring a top layer of graphene onto the as-grown CNTs with direct graphene-to-CNT contact at the interface. The electrical properties of the CNT–graphene contact were characterized by four-point-probe (4PP) I–V measurements of an Au–CNT–graphene–CNT–Au structure. The CNT–graphene contact resistance was benchmarked against the value of CNT–Au under the same fabrication and measurement conditions.

II. Experimental Methods

The major fabrication and assembly steps of the Au–CNT–graphene–CNT–Au structure are summarized in Fig. 1. The fabrication uses the Si substrate with a 280-nm SiO_2 layer deposited using the thermal oxidation technique (Fig. 1, step 1). First, the bottom Au pads (20 nm Ti/100 nm Au) and buffer/catalyst layer (8 nm Al/2 nm Al_2O_3/1.1 nm Fe) were sequentially patterned on a silicon wafer using e-beam evaporation deposition and lift-off process (Fig. 1, step 2). Then, the freestanding CNTs were grown using the thermal chemical vapor deposition (TCVD) method with hydrogen (H_2) and acetylene (C_2H_2) gas flow ratio of 3:1 at 650 °C (Fig. 1, step 3). After CNT growth, two pieces of 80-μm-thick polyethylene terephthalate (PET) with double-side nonconducting adhesives were assembled on the sides of the CNT bundles as the spacers to support the freestanding CNTs when the top graphene layer was transferred (Fig. 1, step 4). Finally, few-layer graphene on the PET (or SiO_2/Si) substrate was flipped over and pressed down onto the CNT bundles (Fig. 1, steps 5 and 6). Graphene

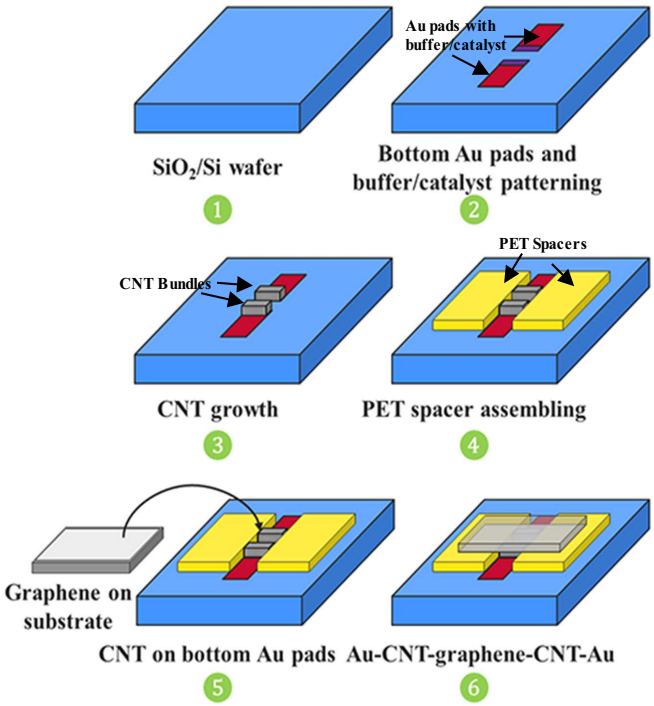

Fig. 1. Fabrication and assembly steps of the Au–CNT–graphene–CNT–Au structure.

with the substrate was attached by the mechanical force of the top adhesive of PET spacers, creating direct contact between the graphene and the CNTs.

The high contact resistance between the CNTs and the metal is always a key issue in the CNT interconnects limiting their feasibility in the application [6], [22]–[24], [33]–[37]. However, significant discrepancies are present in the state-of-the-art values of the CNT–metal contact resistance, due to the absence of standardized techniques for the CNT resistance. In our work, the Au film (on SiO_2/Si substrate) is used as the control sample under identical CNT growth conditions and assembly processes. The 4PP I–V measurements were used to characterize the electrical properties of the graphene and Au bridge structure. The total resistance of the graphene and Au bridge structure can be correspondingly expressed as

$$R_{\text{total}} = R_{\text{btm\_Au}} + 2R_{\text{Au-CNT-G}} + R_{\text{G}} \tag{1}$$

and

$$R_{\text{total}} = R_{\text{btm\_Au}} + 2R_{\text{Au-CNT-Au}} + R_{\text{top\_Au}} \tag{2}$$

where $R_{\text{btm\_Au}}$ is the resistance of the bottom Au pads; $R_{\text{Au-CNT-G}}$ and $R_{\text{Au-CNT-Au}}$ are the resistance of one CNT bump including the contact resistance of CNT–bottom Au, the resistance of the bulk CNT, and the contact resistance of CNT–graphene or CNT–top Au; R_{G} and $R_{\text{top\_Au}}$ are the resistance of the top graphene layer and Au film, respectively. Equations (1) and (2) are established based on the assumption where Au, CNTs, and graphene exhibit similar behavior as Ohmic resistors, connecting in series during electrical conduction.

To extract $R_{\text{Au-CNT-G}}$ and $R_{\text{Au-CNT-Au}}$ in (1) and (2), the values of $R_{\text{btm\_Au}}$, R_{G}, and $R_{\text{top\_Au}}$ need to be determined.

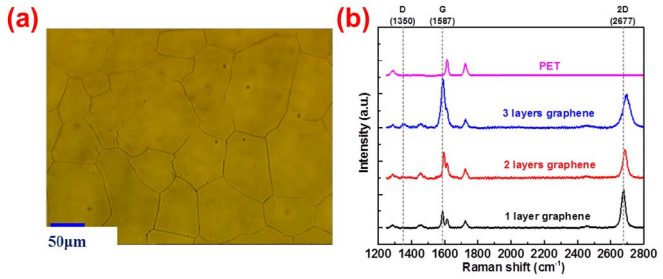

Fig. 2. (a) Optical and (b) Raman images of the graphene on SiO_2/Si and PET.

R_{btm_Au} can be measured from the control groups with the same dimension of the bottom Au pads. R_G and R_{top_Au} can be estimated using the equation of $R = (L/W_{eff})R_S$ (3), where L is the distance between two CNT bundles; W_{eff} is the effective width of the top graphene layer or Au film; R_S is the sheet resistance of the graphene layer or Au film. Nevertheless, to use (1) and (2), the CNT resistance needs to be subtracted. Using the reported CNT resistivity of 9.7–33.8 mΩ · cm [6], [15], the CNT resistance can be determined using the Ohm's law. However, the calculation is carried out based on the assumptions where the current density distribution and the crystallinity across the whole CNT bundles are similar. In actual CNT growth, the discrepancies in crystallinity and current density across various regions of the CNT bundles can be anticipated. Nevertheless, in this work, the overall electrical properties of the CNT bundles are taken into consideration to explore the feasibility of the CNT–graphene heterostructure in TSV interconnect applications.

III. Results and Discussion

The graphene substrates used in this work were intrinsic CVD graphene transferred on the top of PET (or 350 nm SiO_2/Si wafer) with a dimension of 10 mm × 10 mm. The structural characteristics of graphene were confirmed by optical microscopy and Raman characterization as one to three layers of poly-crystal graphene (Fig. 2). On the other hand, 20 nm Ti/100 nm Au was deposited by e-beam evaporation on the 280-nm SiO_2/Si wafer to be used as the control samples compared with the graphene samples. The sheet resistances of the graphene layer and Au film were 218–237 and 0.31–0.32 Ω/sq, respectively, measured by the 4PP sheet resistance measurement system. High sheet resistance of graphene may be attributed to the grain boundaries of the poly-crystal formed during the CVD growth, whereas the observed defects could be induced during the transferring process of the micro-scale area onto the substrate.

Based on (3), R_G will be ~730 times larger than R_{top_Au} with the same dimension (L/W_{eff}), leading to a significant increase in the total resistance of the graphene bridge structure. To reduce the effect of R_G, another configuration of the CNT area (Fig. 3, configuration A) with much smaller distance (L) between two CNT bundles was designed to benchmark against the regular square-shaped CNT area (Fig. 3, configuration B). The size of the CNT area in configurations A and B was maintained at the same value.

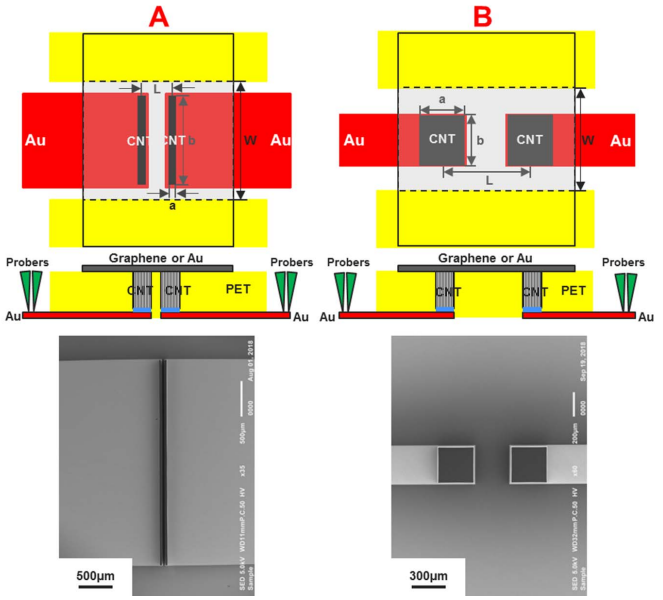

Fig. 3. Schematics and SEM images of two configurations of the CNT area with the same size (left: configuration A, right: configuration B).

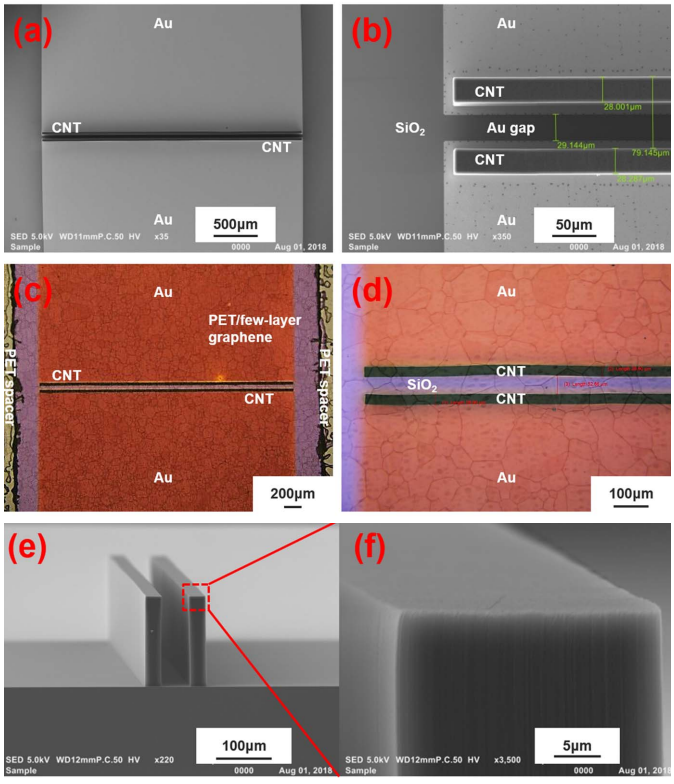

Fig. 4. (a) and (b) SEM images after the CNT growth. (c) and (d) Optical images after top graphene layer transferred. (e) and (f) SEM cross-sectional view of two CNT walls of the dummy sample cut into half.

The optical microscopy and scanning electron microscopy (SEM) images of the fabricated Au–CNT–graphene–CNT–Au structure of configuration A are presented in Fig. 4. As shown in Fig. 4(a) and (b), two CNT walls grown on the top of the bottom Au pads were uniform and

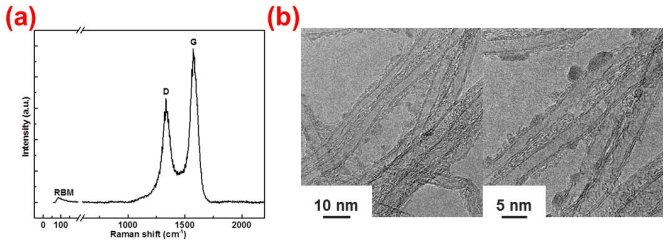

Fig. 5. (a) Raman and (b) transmission electron microscopy (TEM) images of the as-grown CNTs.

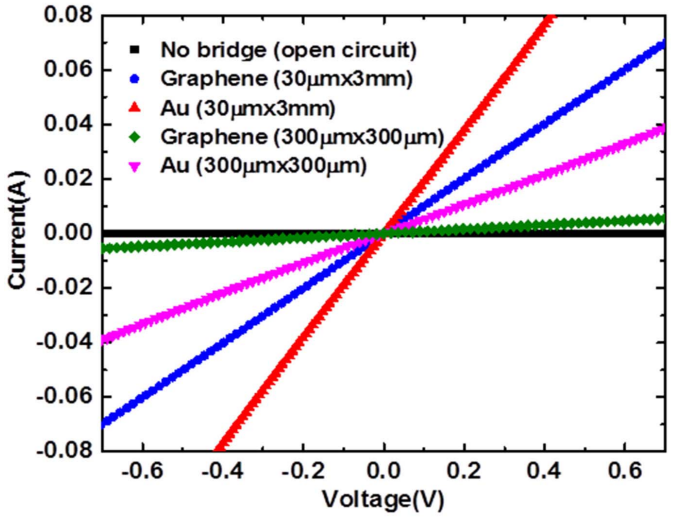

Fig. 6. 4PP I–V measurement results of the total resistance of the graphene and Au bridge structure with two configurations of the CNT area.

well-aligned. Fig. 4(c) and (d) shows the direct contact of the poly-crystal graphene with observable grain boundaries to the CNTs. Meanwhile, the SEM image of the cross-sectional view of the two CNT walls is shown in Fig. 4(e) and (f). The vertical length of the CNTs was fine-tuned to be slightly higher than the thickness of the PET spacers (80 μm). Here, the vertical length of the CNT walls on the real sample was estimated to be around 110 μm (details of the estimation can be found in Appendix A). The I_G/I_D peak ratio and the average diameter of the CNTs were $\sim$1.5 and $\sim$3 nm, respectively, as shown in Fig. 5. The CNT density was estimated as $\sim 10^{11}$ cm^{-2} (details of the density estimation are shown in Appendix B), which is expected to be much higher than the PECVD grown CNTs $\sim 10^{9}$ cm^{-2} [38].

The 4PP I–V measurement is performed on the Au–CNT–graphene–CNT–Au structure with configuration A, as displayed in Fig. 6 (blue-dotted line). It is shown that the current increases linearly under the voltage sweep ranging from -1 to 1 V. The short circuit between two CNT walls or bottom Au pads was excluded by the I–V measurement before graphene transfer. After the transfer of graphene onto the CNTs, the gap between two CNT walls remained as shown in Fig. 4(c) and (d), suggesting the omission of current shortage between two walls after the graphene transfer. Ruling out all possible shortages, it can be postulated that the ohmic contact was achieved between the graphene and CNTs.

The I–V curves of the graphene and Au bridge structure with two different CNT area configurations are shown in Fig. 6. The Au bridge structure shows a linear response to current upon voltage application, similar to its graphene bridge counterpart. However, its total resistance was smaller compared with the value of the graphene bridge structure with the same configuration of the CNT area, possibly due to the significantly large valued of R_G when compared with R_{top_Au}, as mentioned earlier. Meanwhile, for the graphene bridge structure, configuration A (30 μm $\times$ 3 mm) with closer distance (L) between two CNT walls has much smaller total resistance than the value of configuration B (300 μm $\times$ 300 μm) as expected, due to the large R_G in the structure of configuration B.

The measured values of R_{btm_Au} and the estimated values of R_G and R_{top_Au} for various CNT–graphene configurations are listed in Table I. Detailed estimation method of R_G and R_{top_Au} is presented in Appendix C. $R_{Au-CNT-G}$ and $R_{Au-CNT-Au}$ are extracted from (1) and (2) as shown in Table I. Under the same configuration, $R_{Au-CNT-G}$ has similar value with $R_{Au-CNT-Au}$ suggesting that formation of similar ohmic contact was formed at the CNT–graphene interface and at the CNT–top Au interface. The contact between the CNTs and graphene can be possibly achieved by the Van der Waals forces as the current density ($\ll 10^8$ A/cm^2) induced from the I–V measurements is relatively insignificant to fuse the CNTs and graphene with covalent carbon bonds [39]. On the other hand, the contact resistance between the CNTs and graphene was slightly smaller than the contact resistance between the CNTs and Au. A possible reason for this is the low discrepancy in the work functions of graphene/CNTs (4.6 eV/4.7 eV [40]), when compared with Au/CNTs (5.1 eV/4.7 eV), resulting in possible electron tunneling in the CNT–graphene interface. Under identical CNT areas, the contact resistances between the CNTs and graphene (or between the CNTs and Au) of configurations A and B were different. This shows that a nonuniform current density exists at the CNT–graphene (or CNT–Au) contact due to the current crowding effect [41]. The effective contact area of configuration A is larger than configuration B resulting in smaller contact resistance in configuration A. The Ohmic contact obtained aligns well with the assumptions in using (1) and (2), as mentioned in the previous section. As the Ohmic contact can be postulated, the contact resistance can be postulated to increase linearly with reduced contact area, as agreed by the Ohm's law. In other words, a possible increase in the contact resistance may be anticipated for miniaturized interconnects with smaller CNT–graphene contact area. However, in actual CNT–graphene interconnects, more uncertainties shall be considered, such as discrepancies in CNT height/crystallinity across CNTs, which requires further investigations to address these possible discrepancies.

The resistance of one CNT bump ($R_{Au-CNT-G}$) in this work is compared against the results from state of the art as shown in Table II. By normalization of the CNT area, it shows that the obtained outcomes from this work compare favorably with the state of the art [35], [37]. However, as the reported studies used various CNT area dimensions, further study is needed

TABLE I
TOTAL AND EXTRACTED ONE-CNT BUMP RESISTANCE OF THE GRAPHENE AND AU BRIDGE STRUCTURE WITH TWO CONFIGURATIONS OF THE CNT AREA

Configuration	W (mm)	L (mm)	CNT area			R_{total} (Ω)	R_{btm_Au} (Ω)	R_{top_Au} (Ω)	R_G (Ω)	$R_{Au-CNT-G}$ or $R_{Au-CNT-Au}$ (Ω)
			a (mm)	b (mm)	S (mm^2)					
A with graphene bridge (PET)	3.6	0.08	0.03	2.95	0.09	10.0	0.7	/	5.1	2.1
A with Au bridge (SiO_2/Si)	4.5	0.08	0.03	2.96	0.09	5.2	0.7	0.01	/	2.2
B with graphene bridge (SiO_2/Si)	4.2	0.77	0.28	0.28	0.08	128.1	7.0	/	110.7	5.2
B with Au bridge (SiO_2/Si)	3.4	0.61	0.30	0.30	0.09	18.2	7.0	0.12	/	5.5

TABLE II
RESISTANCE OF ONE-CNT BUMP [INCLUDING THE CNT–METAL (CNT–GRAPHENE) CONTACT RESISTANCE] OF THIS WORK AND THE REPORTED STATE OF THE ART

	$R_{Au-CNT-Au}$ [35]	$R_{ZrN-CNT-Al}$ [37]	$R_{Au-CNT-Au}$ [6]	$R_{Au-CNT-G}$ (this work)
CNT bump resistance R (Ω)	280	457	16.1	2.1
CNT area (μm^2)	1963	2827	7854	90000
CNT height (μm)	120	300	132	110

TABLE III
REPEATABILITY TESTS OF THE TOTAL RESISTANCE FOR THE GRAPHENE AND AU BRIDGE STRUCTURE

Sample	R_{total} (Ω)				
	1st	2nd	3rd	4th	5th
A with graphene bridge (PET)	11.1	10.6	**10.0**	10.2	10.0
A with Au bridge (SiO_2/Si)	**5.2**	6.2	7.0	6.8	7.0
B with graphene bridge (SiO_2/Si)	**128.1**	135.4	135.0	135.0	133.7
B with Au bridge (SiO_2/Si)	**18.2**	21.3	21.8	22.3	23.3

to explore the possible factors affecting the CNT–graphene contact resistance with smaller CNT areas.

Repeatability tests of the total resistance were conducted to each graphene and Au bridge structure as shown in Table III. Except for the graphene bridge structure with the PET substrate, the other three structures with the SiO_2/Si substrate show increasing trend in resistances under the repeated voltage sweeps (−1 to 1 V). This can be attributed to the damage of the accumulating charges at the air gap between the CNTs and graphene (or Au) contact. However, for the graphene bridge structure with the PET substrate, the air gap can be shortened by the electrostatic force of the accumulating charges after several voltage sweeps because the PET substrate is flexible. Thus, the total resistance of the graphene bridge structure with the PET substrate decreases initially, and then stabilized with the voltage sweeps repeated.

IV. CONCLUSION

In this article, the transfer process of a top graphene layer onto the as-grown CNT bundles was successfully performed. Direct graphene-to-CNT contact was formed at the CNT–graphene interface. The 4PP I–V characterization suggests that the ohmic contact was formed between the graphene and CNTs. Low CNT bump resistance of 2.1 Ω for 90 000-μm^2 CNT area including the CNT–graphene contact resistance was obtained, demonstrating a reduction in the contact resistance between the CNT and Au under the same fabrication and measurement conditions. This article presents the preliminary results for the assembly process of top-transferred graphene on the CNTs and the electrical properties of the direct CNT–graphene contact. For the future work, the reduced contact resistance enables scaling down of the CNT–graphene interconnects from the investigated 90 000-μm^2 CNT area with improved electrical properties for further exploration, and the bottom Au pads of the bridge structure shall be replaced by the patterned graphene to complete the full-carbon 3-D interconnection.

APPENDIX

A. Estimation of the CNTs' Vertical Length

The vertical length of the CNT walls on the dummy sample was measured directly from the cross-sectional SEM image as shown in Fig. 7(a). The planar length of the CNT walls on the same dummy sample measured from the tilted-view SEM image is shown in Fig. 7(b). From the tilted-view SEM

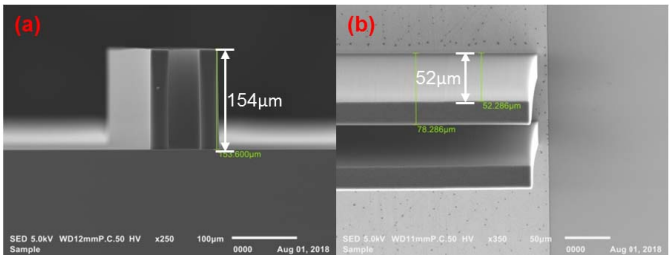

Fig. 7. (a) Cross-sectional SEM image of the vertical length of the CNT walls on the dummy sample. (b) Planar length of the CNT walls on the same dummy sample from the top-view SEM image tilted at 20°.

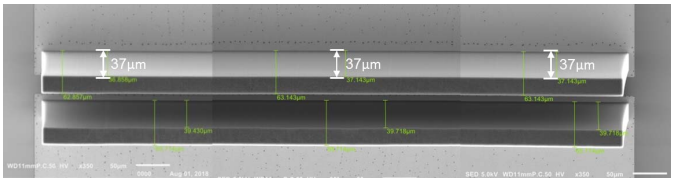

Fig. 8. Planar length of the CNT walls on the real sample from the top-view SEM image tilted at 20°.

image, the planar length of the CNT walls on the real sample was measured as shown in Fig. 8 with satisfactory uniformity. Using the same ratio of the planar and vertical length of the CNTs on the dummy sample, the vertical length of the CNT walls on the real sample can be calculated to be 110 μm.

B. CNT Density Estimation

The average diameter of the CNTs was ~3 nm as shown in the TEM images. Using the following formula, the densities of the CNTs (ρ) can be estimated:

$$\rho = \frac{F \times S}{\pi (d/2)^2}$$

where F is the filling factor ratio (surface area covered with the CNTs after densification/surface area covered with the CNTs before densification), S is the surface area before densification, and d is the average diameter of the CNTs. To determine the filling ratio, bumps of 1 mm^2 were patterned (not shown) on each sample and subjected to the same growth process. The densification process was performed by immersing the sample in isopropyl alcohol (IPA). The filling factor was calculated to be 0.132 ± 0.008 using imaging software pixel calculation, based on more than 10 CNT bumps. Using the above-mentioned technique, the surface density of the CNTs was calculated to be ~10^{11} cm^{-2}.

C. Determination of W_{eff} and Estimation of R_{G} and $R_{\text{top\_Au}}$

R_{G} and $R_{\text{top\_Au}}$ can be estimated using (3): $R = (L/W_{\text{eff}})R_{\text{S}}$, where L is the distance between two CNT bundles; W_{eff} is the effective width of the top graphene layer or Au film; R_{S} is the sheet resistance of the graphene layer or Au film. Based on two configurations of the CNT area and the physical width (W) of the graphene layer or Au film, as shown in Fig. 3 and Table I, it can be postulated as follows.

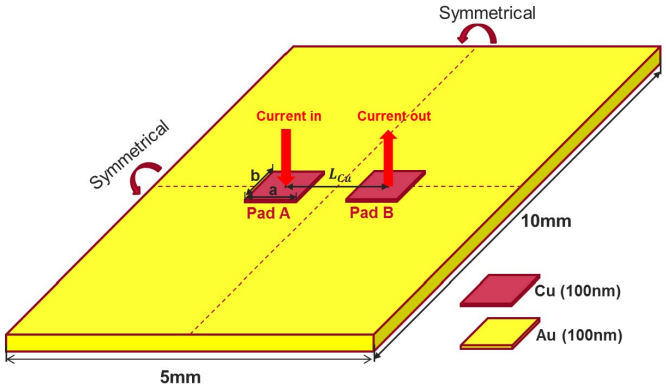

Fig. 9. Illustration of two Cu electrodes replacing the two CNT bundles on the top of the Au film.

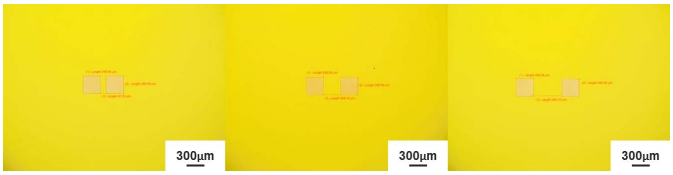

Fig. 10. Optical images of the patterned two Cu electrodes on the Au film with three different values of L_{Cu}.

1) For the CNT area with configuration A, $W_{\text{eff}} \approx W$ because the width b of the CNT area (3 mm) is close to W (3.6 or 4.5 mm) and L (80 μm) is much smaller compared with the value of b (3 mm).
2) For the CNT area with configuration B, $W_{\text{eff}} < W$ because the width b of the CNT area (300 μm) is much smaller than W (4.2 or 3.4 mm) and L (770 or 610 μm) is larger than the value of b (300 μm).

For the CNT area with configuration B, W_{eff} can be determined by the transfer length method (TLM) with two Cu electrodes replacing the two CNT bundles on the top of the Au film with a sample size of 5 mm × 10 mm, as shown in Fig. 9. The total resistance between two Cu electrodes can be expressed as

$$R_{\text{total}} = 2(R_{\text{Cu/Au}} + R_{\text{Cu}}) + \frac{R_{\text{S}}}{W_{\text{eff}}} L_{\text{Cu}}$$

where $R_{\text{Cu/Au}}$ and R_{Cu} are the contact resistance between Cu and Au and the bulk resistance of one Cu electrode, respectively; R_{S} is the sheet resistance of the Au film; L_{Cu} is the distance between two Cu electrodes. By varying the distance between two Cu electrodes, the total resistance versus L_{Cu} will have a linear response. The slope equals to $R_{\text{S}}/W_{\text{eff}}$.

Fig. 10 shows the optical images of the patterned two Cu electrodes on the Au film with three different values of L_{Cu}. Table IV shows the 4PP I–V measured total resistances of different L_{Cu} from three batches of samples. Fig. 11 plots the linear response of the total resistance versus L_{Cu} with a slope 194.3 mΩ/mm. R_{S} of the Au film was measured to be 313 mΩ by the 4PP sheet resistance measurement machine. Subsequently, W_{eff} was calculated to be 1.6 mm (applicable for L within the range of 396–794 μm).

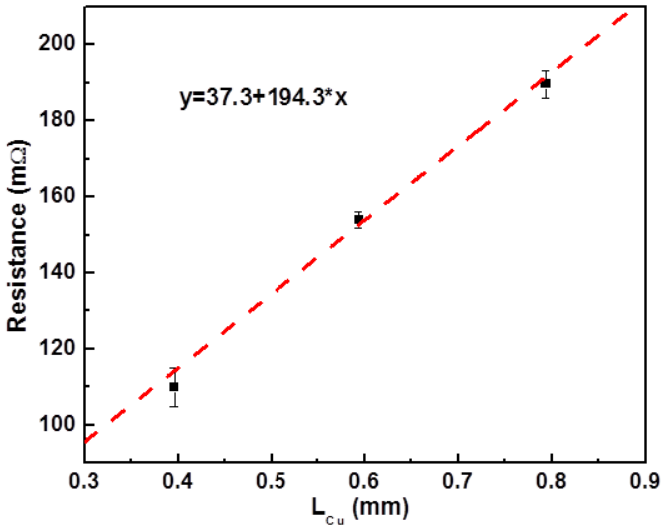

Fig. 11. Linear response of the total resistance versus L_{Cu}.

TABLE IV
4PP I–V MEASURED TOTAL RESISTANCES OF DIFFERENT L_{Cu} FROM THREE BATCHES OF SAMPLES

L_{Cu} (mm)	Resistance (mΩ)		
	Batch 1	Batch 2	Batch 3
0.396	104	113	113
0.594	154	156	152
0.794	186	190	193

ACKNOWLEDGMENT

The authors would like to thank the Center for Micro-/Nano-electronics (NOVITAS), CNRS International Nanyang Technological University (NTU) THALES Research Alliance (CINTRA), and Silicon Technologies Center of Excellence (Si-COE) at NTU, Singapore, for resources. They would also like to thank management and staff in the Nanyang Nano Fabrication Center (N2FC) at NTU, Singapore.

REFERENCES

[1] R. R. Schaller, "Moore's law: Past, present and future," *IEEE Spectr.*, vol. 34, no. 6, pp. 52–59, Jun. 1997.
[2] W. Arden, M. Brillouët, P. Cogez, M. Graef, B. Huizing, and R. Mahnkopf, "ITRS: More-than-Moore," in *Proc. Int. Technol. Roadmap Semicond.*, 2010, pp. 8–11.
[3] R. R. Tummala, "Moore's law meets its match," *IEEE Spectr.*, vol. 43, no. 6, pp. 44–49, Jun. 2006.
[4] P. G. Emma and E. Kursun, "Is 3D chip technology the next growth engine for performance improvement?" *IBM J. Res. Develop.*, vol. 52, pp. 541–552, Nov. 2008.
[5] N. Khan *et al.*, "3-D packaging with through-silicon via (TSV) for electrical and fluidic interconnections," *IEEE Trans. Compon., Packag., Manuf. Technol.*, vol. 3, no. 2, pp. 221–228, Nov. 2013.
[6] T. Wang, K. Jeppson, L. Ye, and J. Liu, "Carbon-nanotube through-silicon via interconnects for three-dimensional integration," *Small*, vol. 7, no. 16, pp. 2313–2317, Aug. 2011.
[7] H. Tong, "Microelectronics packaging: Present and future," *Mater. Chem. Phys.*, vol. 40, pp. 147–161, Apr. 1995.
[8] J. H. Lau, "Overview and outlook of through-silicon via (TSV) and 3D integrations," *Microelectron. Int.*, vol. 28, no. 2, pp. 8–22, May 2011.
[9] Y. Zhu, J. Zhang, H. Y. Li, C. S. Tan, and G. Xia, "Study of near-surface stresses in silicon around through-silicon vias at elevated temperatures by Raman spectroscopy and simulations," *IEEE Trans. Device Mater. Rel.*, vol. 15, no. 2, pp. 142–148, Jun. 2015.
[10] I. De Wolf, K. Croes, and E. Beyne, "Expected failures in 3-D technology and related failure analysis challenges," *IEEE Trans. Compon., Packag., Manuf. Technol.*, vol. 8, no. 5, pp. 711–718, May 2018.
[11] W.-S. Zhao *et al.*, "High-frequency modeling of on-chip coupled carbon nanotube interconnects for millimeter-wave applications," *IEEE Trans. Compon., Packag., Manuf. Technol.*, vol. 6, no. 8, pp. 1226–1232, Aug. 2016.
[12] A. Maffucci, F. Micciulla, A. E. Cataldo, G. Miano, and S. Bellucci, "Modeling, fabrication, and characterization of large carbon nanotube interconnects with negative temperature coefficient of the resistance," *IEEE Trans. Compon., Packag., Manuf. Technol.*, vol. 7, no. 4, pp. 485–493, Apr. 2017.
[13] T. Wang *et al.*, "Through-silicon vias filled with densified and transferred carbon nanotube forests," *IEEE Electron Device Lett.*, vol. 33, no. 3, pp. 420–422, Mar. 2012.
[14] H. Dai, E. Wong, and C. Lieber, "Probing electrical transport in nanomaterials: Conductivity of individual carbon nanotubes," *Science*, vol. 272, no. 5261, pp. 523–526, Apr. 1996.
[15] T. Xu, Z. Wang, J. Miao, X. Chen, and C. M. Tan, "Aligned carbon nanotubes for through-wafer interconnects," *Appl. Phys. Lett.*, vol. 91, no. 4, Jul. 2007, Art. no. 042108.
[16] B. Q. Wei, R. Vajtai, and P. M. Ajayan, "Reliability and current carrying capacity of carbon nanotubes," *Appl. Phys. Lett.*, vol. 79, no. 8, pp. 1172–1174, Aug. 2001.
[17] P. Kim, L. Shi, A. Majumdar, and P. L. McEuen, "Thermal transport measurements of individual multiwalled nanotubes," *Phys. Rev. Lett.*, vol. 87, no. 21, Oct. 2001, Art. no. 215502.
[18] T. Y. Choi, D. Poulikakos, J. Tharian, and U. Sennhauser, "Measurement of thermal conductivity of individual multiwalled carbon nanotubes by the 3-ω method," *Appl. Phys. Lett.*, vol. 87, no. 1, Jun. 2005, Art. no. 013108.
[19] Q. Kong *et al.*, "Thermal conductivity characterization of three dimensional carbon nanotube network using freestanding sensor-based 3ω technique," *Surf. Coatings Technol.*, vol. 345, pp. 105–112, Jul. 2018.
[20] Q. Kong *et al.*, "Novel three-dimensional carbon nanotube networks as high performance thermal interface materials," *Carbon*, vol. 132, pp. 359–369, Jun. 2018.
[21] J.-W. Jiang, J.-S. Wang, and B. Li, "Thermal expansion in single-walled carbon nanotubes and graphene: Nonequilibrium Green's function approach," *Phys. Rev. B, Condens. Matter*, vol. 80, no. 20, Nov. 2009, Art. no. 205429.
[22] J. Vanpaemel *et al.*, "Growth and integration challenges for carbon nanotube interconnects," *Microelectron. Eng.*, vol. 120, pp. 188–193, May 2014.
[23] S. Vollebregt, R. Ishihara, F. Tichelaar, J. Van Der Cingel, and K. Beenakker, "Electrical characterization of carbon nanotube vertical interconnects with different lengths and widths," in *Proc. IEEE Int. Interconnect Technol. Conf. (IITC)*, Jun. 2012, pp. 1–3.
[24] I. Soga *et al.*, "Carbon nanotube bumps for LSI interconnect," in *Proc. 58th Electron. Compon. Technol. Conf.*, May 2008, pp. 1390–1394.
[25] T. Iwai *et al.*, "Thermal and source bumps utilizing carbon nanotubes for flip-chip high power amplifiers," in *IEDM Tech. Dig.*, Dec. 2005, pp. 257–260.
[26] S. Hermann, B. Pahl, R. Ecke, S. E. Schulz, and T. Gessner, "Carbon nanotubes for nanoscale low temperature flip chip connections," *Microelectron. Eng.*, vol. 87, no. 3, pp. 438–442, Mar. 2010.
[27] C. Xu, H. Li, and K. Banerjee, "Modeling, analysis, and design of graphene nano-ribbon interconnects," *IEEE Trans. Electron Devices*, vol. 56, no. 8, pp. 1567–1578, Aug. 2009.
[28] H. Li, C. Xu, N. Srivastava, and K. Banerjee, "Carbon nanomaterials for next-generation interconnects and passives: Physics, status, and prospects," *IEEE Trans. Electron Devices*, vol. 56, no. 9, pp. 1799–1821, Sep. 2009.
[29] D. Sarkar, C. Xu, H. Li, and K. Banerjee, "High-frequency behavior of graphene-based interconnects—Part I: Impedance modeling," *IEEE Trans. Electron Devices*, vol. 58, no. 3, pp. 843–852, Mar. 2011.

[30] D. Sarkar, C. Xu, H. Li, and K. Banerjee, "High-frequency behavior of graphene-based interconnect—Part II: Impedance analysis and implications for inductor design," *IEEE Trans. Electron Devices*, vol. 58, no. 3, pp. 853–859, Mar. 2011.
[31] W. S. Zhao, Y.-F. Liu, Z. Yong, Y. Fang, and W.-Y. Yin, "Modeling and characterization of carbon-based heterogeneous interconnects for 3-D ICs," in *Proc. IEEE Elect. Design Adv. Packag. Syst. Symp. (EDAPS)*, Dec. 2013, pp. 154–157.
[32] J. Jiang, J. Kang, J. H. Chu, and K. Banerjee, "All-carbon interconnect scheme integrating graphene-wires and carbon-nanotube-vias," in *IEDM Tech. Dig.*, Dec. 2017, pp. 342–345.
[33] K. Ghosh, N. Ranjan, Y. K. Verma, and C. S. Tan, "Graphene–CNT hetero-structure for next generation interconnects," *RSC Adv.*, vol. 6, no. 58, pp. 53054–53061, Jun. 2016.
[34] N. Chiodarelli *et al.*, "Integration of vertical carbon nanotube bundles for interconnects," *J. Electrochem. Soc.*, vol. 157, no. 10, pp. K211–K217, Oct. 2010.
[35] T. Wang, K. Jeppson, N. Olofsson, E. E. B. Campbell, and J. Liu, "Through silicon vias filled with planarized carbon nanotube bundles," *Nanotechnology*, vol. 20, no. 48, Nov. 2009, Art. no. 485203.
[36] S. C. Lim *et al.*, "Contact resistance between metal and carbon nanotube interconnects: Effect of work function and wettability," *Appl. Phys. Lett.*, vol. 95, no. 26, Dec. 2009, Art. no. 264103.
[37] S. Vollebregt, S. Banerjee, F. D. Tichelaar, and R. Ishihara, "Carbon nanotubes TSV grown on an electrically conductive ZrN support layer," in *Proc. IEEE Int. Interconnect Technol. Conf. IEEE Mater. Adv. Met. Conf. (IITC/MAM)*, May 2015, pp. 281–283.
[38] C. C. Yap, *Development of Carbon Nanotubes for Interconnects and Nano-Packaging Applications*, Nanyang Technol. Univ., Singapore, 2013.
[39] K. Asaka, M. Karita, and Y. Saito, "Modification of interface structure and contact resistance between a carbon nanotube and a gold electrode by local melting," *Appl. Surf. Sci.*, vol. 257, no. 7, pp. 2850–2853, Jan. 2011.
[40] P. Liu *et al.*, "Measuring the work function of carbon nanotubes with thermionic method," *Nano Lett.*, vol. 8, no. 2, pp. 647–651, Jan. 2008.
[41] S. M. Song and B. J. Cho, "Contact resistance in graphene channel transistors," *Carbon Lett.*, vol. 14, no. 3, pp. 162–170, 2013.

Ye Zhu received the B.S. degree in chemistry from Xiamen University, Xiamen, China, in 2012, and the master's degree from the Department of Materials Engineering, University of British Columbia, Vancouver, BC, Canada, in 2015. She is currently pursuing the Ph.D. degree with the School of Electrical and Electronic Engineering, Nanyang Technological University, Singapore. Her master's thesis focused on the stress analysis of through-silicon via (TSV) in three-dimensional integration circuits (3-D ICs) by micro-Raman spectroscopy and finite element analysis (FEA) simulations. Her Ph.D. thesis mainly focuses on the implementation of full-carbon-based 3-D interconnects.

Chong Wei Tan received the B.Eng. degree in electrical and electronics engineering (EEE), the M.Eng. degree in mechanical aerospace engineering, and the Ph.D. EEE from Nanyang Technological University (NTU), Singapore, in 2005, 2007, and 2015, respectively.

He is currently a Post-Doctoral Research Fellow with the School of Electrical and Electronic Engineering, NTU. His current research interests include carbon-based hybrid materials for MEMS and nanoelectronics applications, thermal management in electronic devices, advanced 3-D interconnect TSV, diamond as substrate for high-power devices, and carbon nanotubes for field emission and RF applications.

Shen Lin Chua received the B.Eng. degree in mechanical and aerospace engineering from Nanyang Technological University (NTU), Singapore, in 2012, where he is currently pursuing the Ph.D. degree.

From 2013 to 2016, he was a Research Assistant with Termasek Laboratories @ NTU, School of Electrical and Electronics Engineering (EEE), NTU. Since 2017, he has been a Project Officer with the Center of Micro-/Nano-electronics (NOVITAS), School of EEE, NTU, where he is currently a Project Officer with Termasek Laboratories @ NTU, Microsystems Technology Development Center. His current research interests include material bonding for 3-D integration, electronics packaging, wafer-to-wafer bonding, and thin-film technologies for CMOS-compatible novel electronic devices.

Yu Dian Lim received the B.Eng. degree in materials and the M.Sc. degree in materials engineering from the University of Malaya (UM), Kuala Lumpur, Malaysia, in 2011 and 2014, respectively, and the Ph.D. degree in electrical and electronics engineering from Nanyang Technological University (NTU), Singapore, in 2018.

He is currently a Post-Doctoral Research Fellow with the School of Electrical and Electronic Engineering, NTU. He has been involved in multidisciplinary research studies, including nanomaterials, nanoelectronics, MEMS fabrication, and communication device design. His current research interests include silicon photonics integrated circuit design, quantum computing devices, and triboelectric nanogenerator (TENG) design and application.

Boris Vaisband received the B.S. degree in computer engineering from the Technion—Israel Institute of Technology, Haifa, Israel, in 2011, and the M.S. and Ph.D. degrees in electrical engineering from the University of Rochester, Rochester, NY, USA, in 2012 and 2017, respectively.

He is currently a Post-Doctoral Scholar with the University of California at Los Angeles, Los Angeles, CA, USA, where he is involved in wafer-level heterogeneous systems integration. His current research interests include integration of heterogeneous systems, communication, power delivery, global interconnects, and thermal-aware design and floor planning.

Beng Kang Tay (SM'19) received the bachelor's degree (Hons.) from the National University of Singapore, Singapore, in 1985, and the Ph.D. degree from Nanyang Technological University (NTU), Singapore, in 1999.

He is currently a Professor with the School of Electrical and Electronics Engineering (EEE), NTU. He is also the Deputy Director for CNRS-International-NTU-Thales Research Alliance (CINTRA). His current research interests include growth and application of carbon-based and 2-D materials for thermal and high-frequency applications.

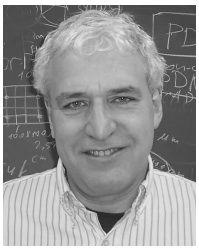

Eby G. Friedman (F'00) received the B.S. degree in electrical engineering from Lafayette College, Easton, PA, USA, in 1979, and the M.S. and Ph.D. degrees in electrical engineering from the University of California at Irvine, Irvine, CA, USA, in 1981 and 1989, respectively.

Since 1991, he has been with the Department of Electrical and Computer Engineering, University of Rochester, Rochester, NY, USA, where he is currently a Distinguished Professor and the Director of the High Performance VLSI/IC Design and Analysis Laboratory.

Dr. Friedman is the Chair of the Steering Committee for the IEEE TRANSACTIONS ON VERY LARGE SCALE INTEGRATION (VLSI) SYSTEMS, a Regional Editor of the *Journal of Circuits, Systems and Computers*, and an Editorial Board Member of *Analog Integrated Circuits and Signal Processing*, the *Microelectronics Journal*, the *Journal of Low Power Electronics*, and the *Journal of Very Large Scale Integration (VLSI) Signal Processing*.

Chuan Seng Tan (SM'19) received the B.Eng. degree in electrical engineering from the University of Malaya, Kuala Lumpur, Malaysia, in 1999, the M.Eng. degree in advanced materials from the National University of Singapore, Singapore, in 2001, and the Ph.D. degree in electrical engineering from the Massachusetts Institute of Technology, Cambridge, MA, USA, in 2006.

He is currently an Associate Professor with the School of Electrical and Electronics Engineering (EEE), Nanyang Technological University (NTU), Singapore. He is also the Associate Dean (Academic) with the College of Engineering, NTU. His current research interests include semiconductor process technology and device physics.

Dr. Tan currently serves as a Committee Member for the International Conference on Wafer Bonding, IEEE-3DIC, IEEE-EPTC, IEEE-ECTC, IEEE-EDTM, IEEE-GFP, and ECS-Wafer Bonding. He was a recipient of the 2019 Exceptional Technical Achievement Award from the IEEE Electronics Packaging Society. He is an Associate Editor of the *Microelectronics Journal (MEJ)* and the IEEE TRANSACTIONS ON COMPONENTS, PACKAGING, AND MANUFACTURING TECHNOLOGY.